

Testing geological proxies for deep-time tidal model simulations

Guo, Bin; Fitzgerald, Laura; Hewitt, Jennifer; Pampaloni, Olivia; Green, Mattias

The Depositional Record

DOI:

[10.1002/dep2.256](https://doi.org/10.1002/dep2.256)

E-pub ahead of print: 18/10/2023

Peer reviewed version

[Cyswllt i'r cyhoeddiad / Link to publication](#)

Dyfyniad o'r fersiwn a gyhoeddwyd / Citation for published version (APA):

Guo, B., Fitzgerald, L., Hewitt, J., Pampaloni, O., & Green, M. (2023). Testing geological proxies for deep-time tidal model simulations. *The Depositional Record*. Advance online publication. <https://doi.org/10.1002/dep2.256>

Hawliau Cyffredinol / General rights

Copyright and moral rights for the publications made accessible in the public portal are retained by the authors and/or other copyright owners and it is a condition of accessing publications that users recognise and abide by the legal requirements associated with these rights.

- Users may download and print one copy of any publication from the public portal for the purpose of private study or research.
- You may not further distribute the material or use it for any profit-making activity or commercial gain
- You may freely distribute the URL identifying the publication in the public portal ?

Take down policy

If you believe that this document breaches copyright please contact us providing details, and we will remove access to the work immediately and investigate your claim.

Testing geological proxies for deep-time tidal model simulations

B. Guo^{1,2}, L. A. M. Fitzgerald¹, J. M. Hewitt¹, O. Pampaloni¹, J. A. M. Green¹

1 School of Ocean Science, Bangor University, Menai Bridge, UK

2 Engineering School, Cardiff University, Cardiff, UK

Author for correspondence: J. A. M. Green, Email: m.green@bangor.ac.uk

Abstract:

Tides are a key driver of a range of Earth system processes, and we now have the capacity to simulate tidal dynamics on a range of temporal and spatial scales. Deep-time tidal model simulations have been used to provide insight into past ocean circulation patterns, evolution of life, and the developments of the Earth-Moon system's orbital configuration. However, these tidal model simulations are relatively poorly constrained and validated because of a lack of readily available proxies. Here, we explore the feasibility of using two types of proxy; (1) sedimentary deposits which can directly estimate palaeotidal ranges, and (2) black shale, to constrain three palaeotidal model simulations for different time slices. Specifically, we use three palaeotidal range proxies for the early Devonian (400 Ma), three palaeotidal range proxies and five black shales for the lower Jurassic (185 Ma), and eight black shales for the early Cretaceous (95 Ma). Both tidal proxies confirm the tidal model results in most locations. The model results for 400 Ma and 185 Ma matched 2/3 of the palaeotidal range proxies for each of these periods. The locations of black shale were compared with tidal front locations predicted by the model outputs based on the Simson-Hunter parameter and the model results from 95 Ma and 185 Ma agree with the black shale proxies in 10/13 of the locations. In the cases where there is a disagreement, the model most likely has a resolution that is too low to fully resolve the details of the coastal topography, or – in one case – the palaeobathymetry is incorrect. Consequently, we argue that it is worth expanding this type of work, and that we can use the data to validate both models and reconstructions.

Keywords: Tides, palaeotidal modelling, tidal proxy, palaeotidal range, tidalites, black shale

1. Introduction

Ocean tides impact a range of Earth system processes. They control the locations of productive shelf sea fronts (Simpson & Hunter, 1974), sustain the climate-regulating global overturning circulation (Wilmes et al., 2021; Wunsch & Ferrari, 2004), drive ocean primary production (Sharples et al., 2007; Tuerena et al., 2019), and set the environment for key evolutionary events (Balbus, 2014; Byrne et al., 2020). The dissipation of tidal energy also slows down Earth's spin and forces the moon to recede to conserve angular momentum (Bills & Ray, 1999; Daher et al., 2021), meaning the tides are a first-order controller of daylength. Recent tidal model results (Green et al., 2017, 2018) show significantly less energetic tides in the past. This has far-reaching consequences for the Earth system, e.g. its biogeochemical cycles, and may have been a driving force in the oxygenation of the atmosphere (Klatt et al., 2021).

Numerical modelling of palaeotides relies on tectonic reconstructions for boundary conditions (see, e.g., Green et al., 2022, and references above). However, despite numerous publications outlining characteristics of palaeotides from the palaeobiological and geological records, numerical simulations are poorly constrained as the proxy information is not readily accessible to the modelling community. Here, we will take a step towards rectifying this by collating information on deep-time tides from different sources and using these data to constrain numerical tidal model simulations for three time slices: 400, 185, and 95 Ma. These were chosen for their representative nature and the availability of suitable proxy data in the literature. The results can also benefit the regional palaeogeographic reconstructions: if the tidal conditions are verified at a location, the regional topography is likely accurate as well.

We obtained palaeotidal range estimations from results presented in the literature; palaeotidal range is determined through palaeoenvironmental interpretation, and may be estimated by analogy to modern tidal environments (Klein, 1971; Wells et al., 2005). For instance, small-scale sedimentary structures are usually distributed in mesotidal environments (Reineck, 1975), while large-scale structures or plane beds are in macrotidal settings (Dalrymple et al., 1990). However, these interpretations may only provide a rough estimation of the tidal range, rather than an accurate definition (Collins et al., 2021).

Furthermore, well-preserved tidalites display ebb-flood, and spring-neap or spring-neap-like cycles, alongside signals of the diurnal inequality, and can be used to constrain days per month and days per year counts in the geological past (Archer, 1996; Coughenour et al., 2009). Under ideal conditions, tidal range in a specific location can be directly estimated from tidalites where complete, fining-upward sequences of sediment are preserved (Devries Klein, 1971; Slingerland, 1986; Tanavsuu-Milkeviciene & Plink-Bjorklund, 2009; Williams, 2000). For example, the sharp contrast of thin neap couplets and thick spring couplets in tidal bundles suggested macrotidal range or higher (Tessier & Gigot, 1989). In other cases, the palaeotidal range could be estimated from the stratigraphic thickness of intertidal deposits in tidal flat units (Klein, 1970, 1971). Sediment can sometimes also be translated into a tidal current range based on bedload transport rates for non-cohesive sediments (Ward et al., 2020), where fine-grained sediments (silt and clay) are more common at low tidal ranges. However, exploring this aspect falls outside the scope of our study, and thus, we will not delve further into it here.

Furthermore, tidal mixing fronts separate a vertically mixed water column from a stratified one (Simpson & Bowers, 1981; Simpson & Hunter, 1974). Their positions are determined by the tidal current magnitude and the water depth, and they are found near contours of

$$\chi = H/u^3 = 200 \quad (1)$$

where H is water depth (m), and u is the tidal current magnitude (m^2/s); χ is commonly referred to as the Simpson-Hunter parameter ($m^{-2} s^3$). Consequently, mapping the fronts provides a proxy for palaeotidal current magnitudes. Black shale deposition occurs in poorly ventilated anoxic conditions incompatible with strong tidal currents (Abdi et al., 2021; He et al., 2022; Stow et al., 2001; Wignall & Newton, 2001). We therefore expect that the presence of a black shale in the geological record will indicate a strongly stratified water column, which can be tracked through the locations of the tidal mixing fronts (Simpson and Hunter, 1974). Note that the specific driver leading to the anoxic event is not important, rather the fact that a well-mixed water column is also well-ventilated and if the water column is mixed, all properties are mixed too. The tides provide a continuous supply of mechanical energy for mixing and we argue that a black shale must sit in a stratified regime. A similar method, tracking microfossil assemblages, has also been suggested but will not be pursued here (Scourse et al., 2002).

To date, a few proof-of-concept studies used tidal deposits to constrain numerical tidal model simulations (e.g., Byrne et al., 2020; Green et al., 2020; Wells et al., 2010; Zuchuat et al., 2022), but the information used was limited to a few data points for specific regions and time slices. Consequently, this paper presents a systematic comparison between environmental proxies and numerical tidal model results.

2. Tidal modelling

The simulations of past tides were made using OTIS – the Oregon State University Tidal Inversion Software – a dedicated tidal model which has been used extensively to simulate deep-time and present day (PD) tides (e.g., Byrne et al., 2020; Egbert et al., 2004; Green et al., 2022). OTIS was benchmarked against other forward tidal models and was shown to perform well (Stammer et al., 2014) which provides a numerical solution to the linearised shallow-water equations forced by the tide only, as presented by the following equation (2) and (3):

$$\frac{\partial \mathbf{U}}{\partial t} + f \times \mathbf{U} = gH \nabla (\eta - \eta_{SAL} - \eta_{EQ}) - \mathbf{F} \quad (2)$$

$$\frac{\partial \eta}{\partial t} - \nabla \cdot \mathbf{U} = 0 \quad (3)$$

Here, $\mathbf{U} = \mathbf{u} H$ is the tidal volume transport (\mathbf{u} is the horizontal velocity vector and H is the water depth (m)), f is the Coriolis parameter (rad/s), g is the acceleration due to gravity (m/s^2), η is the sea-surface elevation (m), η_{SAL} is the self-attraction and loading elevation (m), η_{EQ} is the elevation of the equilibrium tide (m), and \mathbf{F} the tidal energy dissipation term (W/s^2). The dissipation is parameterised through two components, denoted \mathbf{F}_B and \mathbf{F}_W respectively, representing bed friction and energy losses due to tidal conversion, i.e., the energy transferred into a baroclinic tide, respectively. Friction is parameterised using the standard quadratic law, $\mathbf{F}_B = C_D \mathbf{u} |\mathbf{u}|$, where $C_D = 0.003$ is a dimensionless drag coefficient (Taylor, 1920), whereas the tidal conversion term may be written as $\mathbf{F}_W = C \mathbf{U}$, with a conversion coefficient, C , expressed by following equation (4): (Green & Nycander, 2013; Zaron & Egbert, 2006)

$$C(x, y) = \gamma \frac{N_H \bar{N}}{8\pi\omega} (\nabla H)^2 \quad (4)$$

Here, $\gamma = 50$ represents a dimensionless scaling factor representing unresolved bathymetric roughness, N_H is the buoyancy frequency at the seabed (unit of s^{-1}), \bar{N} represents the vertical average of the buoyancy frequency (rad/s), and ω is the frequency of the tide. The buoyancy

frequency, N (rad/s), is given by $N^2 = -g/\rho \partial \rho / \partial z$, where ρ is the density (kg/m^3). The details of the density field are not known for the period we will discuss here, so we used the values of N based on a statistical fit to observed PD values presented by Zaron and Egbert (2006). Consequently, $N(x,y) = 0.00524 \exp(-z/1300)$, where z is the vertical coordinate (m), and the constants 0.00524 and 1300 have units of s^{-1} and m , respectively. The model results are relatively insensitive to changes in stratification and we will not explore this parameter space further (Egbert et al., 2004; Byrne et al., 2020; Green et al., 2020).

2.1 Reconstructions and simulations

The palaeo-bathymetry data came from Scotese & Wright (2018) and was supplied at $1/10^\circ$ horizontal resolution in both latitude and longitude. All bathymetries effectively ran from $89^\circ S$ to $89^\circ N$ in latitude due to the introduction of land at the poles to handle the convergence of the model grid cells at high latitudes. Note that outside of near-resonant states, tidal simulations are relatively insensitive to small-scale topographic changes and the blocking of the poles (Egbert et al., 2004; Wilmes & Green, 2014). The details for each era are summarised below and described in more detail in each section.

All time slices were simulated for the M_2 , S_2 , and K_1 constituents. All time slices were simulated using PD tidal forcing as well as changed forcing to parameters relevant for each time slice (Daher et al., 2021) – see

Table 1 for details. The model outputs the amplitudes and phases of the surface elevations, η , and transports, \mathbf{U} , for each of the constituents.

3. Proxies

Two types of tidal proxies are explored here: (1) sedimentary deposits that can be used to directly estimate palaeotidal range and (2) black shale (BS), which can indirectly estimate tidal conditions.

3.1 Direct proxies: palaeotidal range

Here, we regard palaeotidal ranges interpreted from tidal deposits in the literature as ‘direct proxies’ (DP); these have been used previously to constrain palaeotidal modelling (e.g. Byrne et al., 2020; Green et al., 2020; Zuchuat et al., 2022). We categorised tidal ranges from the literature into the four standard categories: microtidal (0-2 m), mesotidal (2-4 m), macrotidal (4-6 m), and hypertidal (> 6 m) (Archer, 2013). In this investigation, if the results from the tidal model for a proxy location fall within the category provided by the proxy, the simulation is considered accurate. Palaeotidal range proxies will be used to validate the simulations for 400 Ma and 185 Ma. Details of the direct tidal proxies are summarised below and in Supplementary Material tables A and B and the locations are presented in Figure 1(a)-(b).

Three palaeotidal range proxies for 400 Ma were found in the literature, all also used by Byrne et al. (2020); note that the simulations here use a different reconstruction and higher resolution than Byrne et al. (2020) did. A meso–macrotidal regime was discovered in the fine to coarse-grained, tide-dominated deltaic deposits of the Rezekne and Pärnu formations in the Devonian Baltic Basin; these make up (Direct proxy 1) DP1 (our Figure 1(a) and Tanavsuu-Milkeviciene & Plink-Bjorklund, 2009; Tovmasjana, 2013). Another meso–macrotidal environment was found in the rippled and cross-bedded silicilastic and dolomitic tidal flat facies of the Padeha Formation in the Tabas Block of the Central-East Iranian Microcontinent (DP2; Wendt et al., 2004; Zand-Moghadam et al., 2014). Griffing et al. (2000) and Rust et al. (1989) inferred a mesotidal regime from the tidally-deposited sandstone and mudstone

bodies in the Cap-aux-Os Member of the Battery Point Formation in the Catskill Clastic Wedge, Canada (DP3 in Figure 1(a)).

For the 185 Ma time slice, three direct proxies were found in the literature (see Figure 1(b)). Sellwood (1972) determined the minimum tidal range as 1 m from the thickness of sandstone channel-fill sequences in Gry's Lower Coal Series in Bornhom, Denmark (DP4). A macrotidal regime was concluded based on the dimensions of estuarine bedforms in the incised valleys of the Ostreaelv Formation (DP5) in the Niell Klint Group in Jameson Land, Greenland (Ahokas et al., 2014). Lastly, the Helsingborg Member of the Gassum Formation in southern Sweden and the Galgeløkke Member of the Rønne Formation on Bornholm (both combined as DP6) consisting of tidal flat and channel facies, were deposited in a micro- to mesotidal environment (Nielsen et al., 1989).

3.2 Indirect proxies: black shale

It has been suggested that tidal rhythmites, which can indicate palaeotidal range, are predominantly formed within middle to inner estuaries (Tessier, 2023). This can introduce uncertainties when validating tidal model results because the reconstruction is unlikely to cover small scale estuaries. Furthermore, the tidal regimes we have found direct proxies for are almost all meso-macrotidal, leaving us without proxies (at this stage) for low tidal ranges. To address this, it is proposed that locations of black shale constitute an additional tidal proxy for tides in a shelf sea setting.

Black shale is an indirect proxy which can ultimately constrain tidal current velocities. Tide-driven mixing controls stratification in shelf seas, with a tidal mixing front marking the point between vertically mixed and stratified areas as discussed in the introduction. Mapping front positions from the model output and comparing them to locations with black shale therefore constitutes a validation metric: the shale must sit on the stratified side of the front and if they do not, the model simulation is most likely incorrect. The identified palaeo-locations of the black shale formations used here are shown as 'BS' in Figure 1(b)-(c). A total of 13 locations were identified: 5 for the 185 Ma timeslice and a further 8 for 95 Ma. Note that black shale deposits in deep water will not be considered here, as anoxia in the deep ocean is not controlled by tides. Furthermore, black shale deposited between the Precambrian (400 Ga)

to the Devonian (419-358 Ma) was deposited at a time when ocean chemistry was significantly different and there is evidence to suggest that there was not enough oxygen in the marine environment to form oxic waters (Aharon, 2005; Kimura & Watanabe, 2001).

4. Results

4.1 Present day model validation

The performance of the present day set-up of the tidal model was evaluated compared to the TPX09 satellite altimetry constrained product (Egbert & Erofeeva, 2002). The predicted M_2 and S_2 tidal amplitudes for PD are presented in Figure 2, with the globally spatial-averaged root-mean-square (RMS) errors for M_2 and S_2 amplitudes calculated to be 9.8 cm and 4.4 cm, respectively.

4.2 400 Ma

The predicted M_2 and S_2 amplitudes and the mean spring tidal range at 400 Ma are presented in Figure 3 (a) and (b). A region with high amplitudes of M_2 and S_2 is situated in the western and northern parts of Laurussia, southern Siberia, and the northeast of Gondwana, where the M_2 amplitude exceeds 1.5 m, while S_2 amplitude exceeds 1 m. Less energetic waters are found in east Laurussia and northern Siberia as M_2 or S_2 microtidal regimes dominate these areas. The model prediction here is generally consistent with the lower-resolution simulations for 400 Ma from Byrne et al. (2020), but variations in tidal predictions occur in specific areas due to differences in the utilised palaeobathymetry data. For instance, this study reveals significantly higher M_2 amplitudes in southern Siberia (up to 2.5 m) and lower S_2 amplitudes in northeast Laurussia (lower than 0.5 m) compared to the prediction from Byrne et al. (2020).

The mean spring tide range is computed as $2(\eta_{M2} + \eta_{S2})$, as shown in Figure 3(c) and (d), where η_{M2} and η_{S2} are the corresponding tidal amplitudes for principal lunar semidiurnal (M_2) and principal solar semidiurnal (S_2). Macrotidal areas (4-6 m) are located along the west and north coastline of Laurussia, southern Siberia, and northeast region of Gondwana. In contrast, mesotidal regions (2-4 m range) were found on the southeast coast of Laurussia. Compared with direct tidal proxies collected for 400 Ma and plotted in Figure 4, the model prediction

matches reasonably well with the proxies at DP3 and DP2 (see Table A for details). However, the simulation does not agree with the tidal proxy of the DP1. DP1 was located in a meso-macrotidal delta, whereas the simulation indicates a microtidal environment in that region. This discrepancy may be an effect of model resolution: the Pärnu and Rēzekne Formations were deposited in transitional fluvial-tide-dominated flats, tidal channels or in a deltaic distributary channel that, at the current model resolution, is not resolved.

4.3 185 Ma

The 185 Ma model results are validated using both tidal range proxies and black shale (see Supplementary Material Table B for a summary of proxy information). It should be noted that DP4 (Gry's Lower Coal Series) will not work as a tidal proxy because it is too far inland. This is of course still useful information because it tells us that the reconstruction needs to be modified to encompass the proxy location. These simulations host a relatively weak global tide, except for a macrotidal regime in the western Tethys Sea (see Figure 5). It can be argued that if DP4 is moved to the nearest coastal grid cell, it fits well with the tidal model result of 1.4 m M_2 tidal range (Figure 6). The predicted tidal range at DP6 (Helsingborg Member of the Gassum Formation and the Galgeløkke Member of the Rønne Formation) is 1.25 m, which is in the range of the tidal proxy there (Figure 6). However, the tidal range prediction at the DP5 site (Ostreaelv Formation) is 0.30 m, which is a considerable underestimate compared to the 4-6 m macrotidal range that was identified in the proxy. We propose that this is another resolution issue with the model grid: a macrotidal range in a shallow seaway may not be fully resolved with a $1/10^\circ$ model resolution, resulting in the oversight of a likely resonant feature in the inner part of the seaway.

The calculated Simpson-Hunter criterion for 185 Ma in Figure 7 and Table 2 shows that the model result matches four out of five black shale tidal proxies (BS2-BS5). BS1 is located at a borderline mixed region with a value of $\log_{10} \chi \sim 2$ in the model simulations, whereas the proxy of course points to a stratified water column. This could be remedied by increasing the depth of the area to reduce current speeds and increase χ , as demonstrated by equation (1). Again, the tidal proxies give information about the quality of the tectonic reconstructions as well as acting as a validation tool for the tides.

270 4.4 95 Ma

271 The predicted M_2 amplitude and its corresponding velocity magnitude for the 95 Ma time
272 slice are presented in Figure 8. In general, this is a quiescent time slice, with weak tides in the
273 vast epeiric seas covering PD Africa, Asia, and Europe. The exceptions are high-velocity zones
274 northeast of PD Madagascar and north Australia (Figure 8(a)).

275

276 There is a lack of direct tidal proxies for 95 Ma and instead we will use the Simpson-Hunter
277 criterion and black shale formations as proxies. The results shown in Figure 9 indicate that
278 much of the 95 Ma shelf seas were stratified and that the black shale records are matched by
279 the modelled stratification in 6 out of 8 locations (see

Table 3). The two mismatched locations, BS10 and BS12, are again located at the boundary of mixed and stratified regions with values of $\log_{10}\chi = 2.0$ and 1.8, respectively. A small correction of the depth would also ensure a stratified water column at these two locations. The positive correlation between black shale palaeo-locations and tidal front locations suggests that black shale can serve as indirect proxies for palaeotides.

5. Discussion and conclusions

We present simulations of the tides for three deep-time time slices and validate the results with two types of geological tidal proxies: palaeotidal ranges deduced from tidal deposits (a direct proxy) and black shale (an indirect proxy). We collected direct proxies from published literature for 400 Ma and 185 Ma; for both time slices, the model performed reasonably well with proxies agreeing in 2/3 of the locations. However, in areas where it fell short, we argue that the bathymetry of the reconstruction could be modified to ensure a better fit. Using direct proxies is the preferred method for validating palaeotidal models (Byrne et al., 2020; Zuchuat et al., 2022) but they are rare in the literature. Therefore, we propose to use black shale as an indirect proxy, providing an upper limit of the tidal current speeds, and we present a proof-of-concept study for time slices at 185 Ma and 95 Ma. Because of the interconnections between tidal current speeds, stratification, and potential for anoxia, we argue that in cases where the Simpson-Hunter parameter denotes a stratified water column (i.e., $\log_{10}\chi > 2-2.3$), the presence of black shale in that region can be attributed to the water-mass stratification. The results and proxies agree in 10 out of 13 locations across both time slices. It would be easy to change the water depth until the model and proxies agree. This way, we obtain both verified tidal model simulations and improved reconstructions.

The main uncertainty in this type of work is in the bathymetric reconstructions because the tidal dynamics is largely controlled by the bathymetry (Zuchuat et al., 2001; Green et al 2017; 2020; Byrne et al., 2021). The uncertainty or error of the model simulations is given by the RMS value we provide; this also highlights that the main uncertainty is the bathymetry. It is very difficult to quantify the uncertainty or accuracy of the proxies, because they are proxies and we are largely missing modern analogues. However, we feel that this is largely mitigated

here by the range of the tidal characteristics from the proxies and we argue that if the model simulation falls within that range, we can be confident in the results for both the model and the proxy. The problem is when the two don't agree and at least one of the two – the model or the proxy – is incorrect. We have no idea of knowing which one at this stage, and more work is needed to improve the model set up, e.g., by using higher resolution in the model simulations and constraining the reconstructions better. This work is underway and left for a future publication.

Whilst we can argue that the results make sense from a dynamical perspective, the encouraging correlations between the model results and proxies show that the model is reasonably correct, and that the methodology works. It also demonstrates that there could be a wealth of viable tidal proxies available in the literature, and that collecting and collating them is a worthy effort to constrain deep-time tidal model simulations. Two kinds of proxies were explored here, and we argue that it is worth investigating further potential proxies found in the literature. For example, grain size distributions could be used alongside bedforms, such as ripples, to provide direct constraints on the current speed (Baas, 1999; Davis & Dalrymple, 2011; Oost & Baas, 1994). Other proxies can come from palaeobiology, where species distributions can tell us about the size of intertidal zones (and hence tidal range) and, again, help constrain the bathymetry. Matching information of geological formations and basins can also contain estimates of shelf width and specific topography which can be used to further reconstruct bathymetries. The same is true for palaeocurrent directions which could potentially be used to verify shoreline trends. These investigations are left for future publications.

Data availability

The model bathymetries and associated model outputs, along with Matlab scripts to read the files, are available from [10.5281/zenodo.7684234](https://doi.org/10.5281/zenodo.7684234).

Acknowledgement

Simulations were done on Supercomputing Wales with funding from HEFCW. BG and JAMG acknowledge funding from the Natural Environment Research Council (MATCH, NE/S009566/1). LAMF, JMH, and OP were recipients of a 2021 Bangor University

343 Undergraduate internship; they contributed equally to the manuscript and are listed in
344 alphabetical order. We express our sincere gratitude for the constructive and insightful
345 comments provided by Valentin Zuchuat, an anonymous reviewer, and the editors.
346

References

- Abdi, Z., Rimmer, S.M., Rowe, H.D. & Nordeng, S. (2021) Controls on organic matter accumulation in the Bakken Formation, Williston Basin, USA. *Chemical Geology*, 586(October), 120588. <https://doi.org/10.1016/j.chemgeo.2021.120588>.
- Aharon, P. (2005) Redox stratification and anoxia of the early Precambrian oceans: Implications for carbon isotope excursions and oxidation events. *Precambrian Research*, 137(3–4), 207–222. <https://doi.org/10.1016/j.precamres.2005.03.008>.
- Ahokas, J.M., Nystuen, J.P. & Martinus, A.W. (2014) Stratigraphic signatures of punctuated rise in relative sea-level in an estuary-dominated heterolithic succession: Incised valley fills of the Toarcian Ostreelv Formation, Neill Klint Group (Jameson Land, East Greenland). *Marine and Petroleum Geology*, 50, 103–129. <https://doi.org/10.1016/j.marpetgeo.2013.11.001>.
- Archer, A.W. (1996) Reliability of lunar orbital periods extracted from ancient cyclic tidal rhythmites. *Earth and Planetary Science Letters*, 141(1–4), 1–10. [https://doi.org/doi:DOI: 10.1016/0012-821X\(96\)00063-5](https://doi.org/doi:DOI:10.1016/0012-821X(96)00063-5).
- Archer, A. W. (2013). World's highest tides: Hypertidal coastal systems in North America, South America and Europe. *Sedimentary Geology*, 284, 1-25. <https://doi.org/10.1016/j.sedgeo.2012.12.007>
- Baas, J. H. (1999). An empirical model for the development and equilibrium morphology of current ripples in fine sand. *Sedimentology*, 46(1), 123-138. <https://doi.org/10.1046/j.1365-3091.1999.00206.x>
- Baas, J.H., Malarkey, J., Lichtman, I.D., Amoudry, L.O., Thorne, P.D., Hope, J.A., Peakall, J., Paterson, D.M., Bass, S.J., Cooke, R.D. & Manning, A.J. (2021) Current- and Wave-Generated Bedforms on Mixed Sand–Clay Intertidal Flats: A New Bedform Phase Diagram and Implications for Bed Roughness and Preservation Potential. *Frontiers in Earth Science*, 9, 1–27. <https://doi.org/10.3389/feart.2021.747567>.
- Balbus, S.A. (2014) Dynamical, biological and anthropic consequences of equal lunar and solar angular radii. *Proceedings of the Royal Society A: Mathematical, Physical and Engineering Sciences*, 470(2168), 20140263. <https://doi.org/10.1098/rspa.2014.0263>.
- Bills, B.G. & Ray, R.D. (1999) Lunar orbital evolution: A synthesis of recent results. *Geophysical Research Letters*, 26(19), 3045–3048. <https://doi.org/10.1029/1999GL008348>.

379 Bjerstedt, Thomas.W. (1987) Trace fossils indicating estuarine deposystems for the
380 Devonian-Mississippian Cloyd Conglomerate Member, Price Formation, Central
381 Appalachians. *Palaios*, 2(4), 339–349.
382 <https://doi.org/https://doi.org/10.2307/3514759>.

383 Blackledge, B.W., Green, J.A.M., Barnes, R. & Way, M.J. (2020) Tides on Other Earths:
384 Implications for Exoplanet and Palaeo-Tidal Simulations. *Geophysical Research Letters*,
385 47(12). <https://doi.org/10.1029/2019GL085746>.

386 Bowers, D.G. & Simpson, J.H. (1987) Mean position of tidal fronts in European-shelf seas.
387 *Continental Shelf Research*, 7(1), 35–44. [https://doi.org/10.1016/0278-4343\(87\)90062-](https://doi.org/10.1016/0278-4343(87)90062-8)
388 8.

389 Byrne, H.M., Green, J.A.M., Balbus, S.A. & Ahlberg, P.E. (2020) Tides: A key environmental
390 driver of osteichthyan evolution and the fish-tetrapod transition? *Proceedings of the*
391 *Royal Society A: Mathematical, Physical and Engineering Sciences*, 476(2242).
392 <https://doi.org/10.1098/rspa.2020.0355>.

393 Cochonat, T.M.P. (1996) Classification of offshore mass movements. *Journal of Sedimentary*
394 *Research*, 66(1), 43–57. [https://doi.org/https://doi.org/10.1306/D42682AC-2B26-](https://doi.org/https://doi.org/10.1306/D42682AC-2B26-11D7-8648000102C1865D)
395 11D7-8648000102C1865D.

396 Collins, D.S., Avdis, A., Wells, M.R., Dean, C.D., Mitchell, A.J., Allison, P.A., Johnson, H.D.,
397 Hampson, G.J., Hill, J. & Piggott, M.D. (2021) Prediction of shoreline–shelf depositional
398 process regime guided by palaeotidal modelling. *Earth-Science Reviews*, 223, 103827.
399 <https://doi.org/10.1016/j.earscirev.2021.103827>.

400 Tessier, C.L., Archer, A.W. & Lacovara, K.J. (2009) Tides, tidalites, and secular changes in the
401 Earth-Moon system. *Earth-Science Reviews*, 97(1–4), 59–79.
402 <https://doi.org/10.1016/j.earscirev.2009.09.002>.

403 Daher, H., Arbic, B.K., Williams, J.G., Ansong, J.K., Boggs, D.H., Müller, M., Schindelegger, M.,
404 Austermann, J., Cornuelle, B.D., Crawford, E.B., Fringer, O.B., Lau, H.C.P., Lock, S.J.,
405 Maloof, A.C., Menemenlis, D., Mitrovica, J.X., Green, J.A.M. & Huber, M. (2021) Long-
406 Term Earth-Moon Evolution With High-Level Orbit and Ocean Tide Models. *Journal of*
407 *Geophysical Research: Planets*, 126(12), e2021JE006875.
408 <https://doi.org/10.1029/2021je006875>.

- Dalrymple, R. W., Knight, R. J., Zaitlin, B. A., & Middleton, G. V. (1990). Dynamics and facies model of a macrotidal sand-bar complex, Cobequid Bay—Salmon River Estuary (Bay of Fundy). *Sedimentology*, 37(4), 577-612.
<https://doi.org/10.1111/j.1365-3091.1990.tb00624.x>
- Davies, H.S., Duarte, J.C. & Green, J.A.M. (2019) Back to the Future II: Tidal evolution of four supercontinent scenarios. *Earth System Dynamics Discussions*, (October), 1–18.
<https://doi.org/10.5194/esd-2019-61>.
- Davis, R. A., & Dalrymple, R. W. (Eds.). (2012). Principles of tidal sedimentology. Springer, New York. <https://doi.org/10.1007/978-94-007-0123-6>
- Devries Klein, G. (1971) A sedimentary model for determining paleotidal range. *Bulletin of the Geological Society of America*, 82(9), 2585–2592. [https://doi.org/10.1130/0016-7606\(1971\)82\[2585:ASMFDP\]2.0.CO;2](https://doi.org/10.1130/0016-7606(1971)82[2585:ASMFDP]2.0.CO;2).
- Egbert, G.D., & Erofeeva, S.Y. (2002). Efficient inverse modeling of barotropic ocean tides. *Journal of Atmospheric and Oceanic technology*, 19(2), 183-204.
[https://doi.org/10.1175/1520-0426\(2002\)019<0183:EIMOBO>2.0.CO;2](https://doi.org/10.1175/1520-0426(2002)019<0183:EIMOBO>2.0.CO;2)
- Egbert, G.D. & Ray, R.D. (2001) Estimates of M2 tidal energy dissipation from TOPEX/Poseidon altimeter data. *Journal of Geophysical Research: Oceans*, 106(C10), 22475–22502. <https://doi.org/10.1029/2000jc000699>.
- Egbert, G.D., Ray, R.D. & Bills, B.G. (2004) Numerical modeling of the global semidiurnal tide in the present day and in the last glacial maximum. *Journal of Geophysical Research: Oceans*, 109(C3), 1–15. <https://doi.org/10.1029/2003JC001973>.
- Elderbak, K., Leckie, R.M. & Tibert, N.E. (2014) Paleoenvironmental and paleoceanographic changes across the Cenomanian-Turonian Boundary Event (Oceanic Anoxic Event 2) as indicated by foraminiferal assemblages from the eastern margin of the Cretaceous Western Interior Sea. *Palaeogeography, Palaeoclimatology, Palaeoecology*, 413, 29–48.
<https://doi.org/10.1016/j.palaeo.2014.07.002>.
- Forster, A., Kuypers, M.M.M., Turgeon, S.C., Brumsack, H.J., Petrizzo, M.R. & Sinninghe Damsté, J.S. (2008) The Cenomanian/Turonian oceanic anoxic event in the South Atlantic: New insights from a geochemical study of DSDP Site 530A. *Palaeogeography, Palaeoclimatology, Palaeoecology*, 267(3–4), 256–283.
<https://doi.org/10.1016/j.palaeo.2008.07.006>.

440 Gómez, J.J., Comas-Rengifo, M.J. & Goy, A. (2016) The hydrocarbon source rocks of the
 441 Pliensbachian (Early Jurassic) in the Asturian Basin (northern Spain): Their relationship
 442 with the palaeoclimatic oscillations and gamma-ray response. *Journal of Iberian*
 443 *Geology*, 42(3), 259–273. <https://doi.org/10.5209/JIGE.53265>.
 444 Green, J.A.M., Davies, H.S., Duarte, J.C., Creveling, J.R. & Scotese, C. (2020) Weak tides
 445 during Cryogenian glaciations. *Nature Communications*, 11(1).
 446 <https://doi.org/10.1038/s41467-020-20008-3>.
 447 Green, J.A.M. & Duarte, J.C. (Eds.). (2022) A Journey Through Tides. Elsevier.
 448 <https://doi.org/10.1016/C2020-0-02539-9>
 449 Green, J.A.M. & Huber, M. (2013) Tidal dissipation in the early Eocene and implications for
 450 ocean mixing. *Geophysical Research Letters*, 40(11), 2707–2713.
 451 <https://doi.org/10.1002/grl.50510>.
 452 Green, J.A.M., Huber, M., Waltham, D., Buzan, J. & Wells, M. (2017) Explicitly modelled
 453 deep-time tidal dissipation and its implication for Lunar history. *Earth and Planetary*
 454 *Science Letters*, 461, 46–53. <https://doi.org/10.1016/j.epsl.2016.12.038>.
 455 Green, J.A.M., Molloy, J.L., Davies, H.S. & Duarte, J.C. (2018) Is There a Tectonically Driven
 456 Supertidal Cycle? *Geophysical Research Letters*, 45(8), 3568–3576.
 457 <https://doi.org/10.1002/2017GL076695>.
 458 Green, J.A.M. & Nycander, J. (2013) A comparison of tidal conversion parameterizations for
 459 tidal models. *Journal of Physical Oceanography*, 43(1). [https://doi.org/10.1175/JPO-D-](https://doi.org/10.1175/JPO-D-12-023.1)
 460 [12-023.1](https://doi.org/10.1175/JPO-D-12-023.1).
 461 Green, R.H., Lowe, Ryan.J. & Buckley, Mark.L. (2018) Hydrodynamics of a Tidally Forced
 462 Coral Reef Atoll. *Journal of Geophysical Research: Oceans*, 123(10), 7084–7101.
 463 <https://doi.org/10.1029/2018JC013946>.
 464 Griffing, D. H., Bridge, J. S., & Hotton, C. L. (2000). Coastal-fluvial palaeoenvironments and
 465 plant palaeoecology of the Lower Devonian (Emsian), Gaspé Bay, Québec, Canada.
 466 Geological Society, London, Special Publications, 180(1), 61-84.
 467 <https://doi.org/10.1144/GSL.SP.2000.180.01.05>
 468 Hallam, A. & Wignall, P.B. (1999) Mass extinctions and sea-level changes. *Earth Science*
 469 *Reviews*, 48(4), 217–250. [https://doi.org/10.1016/S0012-8252\(99\)00055-0](https://doi.org/10.1016/S0012-8252(99)00055-0).
 470 He, T., Wignall, P.B., Newton, R.J., Atkinson, J.W., Keeling, J.F.J., Xiong, Y. & Poulton, S.W.
 471 (2022) Extensive marine anoxia in the European epicontinental sea during the end-

472 Triassic mass extinction. *Global and Planetary Change*, 210(February), 103771.
 473 <https://doi.org/10.1016/j.gloplacha.2022.103771>.

474 Ikeda, M., Hori, R.S., Ikehara, M., Miyashita, R., Chino, M. & Yamada, K. (2018) Carbon cycle
 475 dynamics linked with Karoo-Ferrar volcanism and astronomical cycles during
 476 Pliensbachian-Toarcian (Early Jurassic). *Global and Planetary Change*, 170, 163–171.
 477 <https://doi.org/10.1016/j.gloplacha.2018.08.012>.

478 Jarvis, I., Lignum, J.S., Grcke, D.R., Jenkyns, H.C. & Pearce, M.A. (2011) Black shale
 479 deposition, atmospheric CO₂ drawdown, and cooling during the Cenomanian-Turonian
 480 Oceanic Anoxic Event. *Paleoceanography*, 26(3).
 481 <https://doi.org/10.1029/2010PA002081>.

482 Jones, E.J.W., Bigg, G.R., Handoh, I.C. & Spathopoulos, F. (2007) Distribution of deep-sea
 483 black shales of Cretaceous age in the eastern Equatorial Atlantic from seismic profiling.
 484 *Palaeogeography, Palaeoclimatology, Palaeoecology*, 248(1–2), 233–246.
 485 <https://doi.org/10.1016/j.palaeo.2006.12.006>.

486 Kadiri, M., Zhang, H., Angeloudis, A. & Piggott, M.D. (2021) Evaluating the eutrophication
 487 risk of an artificial tidal lagoon. *Ocean and Coastal Management*, 203.
 488 <https://doi.org/10.1016/j.ocecoaman.2020.105490>.

489 Kassem, A.A., Sharaf, L.M., Baghdady, A.R. & El-Naby, A.A. (2020) Cenomanian/Turonian
 490 oceanic anoxic event 2 in October oil field, central Gulf of Suez, Egypt. *Journal of*
 491 *African Earth Sciences*, 165. <https://doi.org/10.1016/j.jafrearsci.2020.103817>.

492 Kimura, H. & Watanabe, Y. (2001) Oceanic anoxia at the Precambrian-Cambrian boundary.
 493 *Geology*, 29(11), 995–998. [https://doi.org/https://doi.org/10.1130/0091-](https://doi.org/https://doi.org/10.1130/0091-7613(2001)029<0995:OAATPC>2.0.CO;2)
 494 [7613\(2001\)029<0995:OAATPC>2.0.CO;2](https://doi.org/https://doi.org/10.1130/0091-7613(2001)029<0995:OAATPC>2.0.CO;2).

495 Klatt, J.M., Chennu, A., Arbic, B.K., Biddanda, B.A. & Dick, G.J. (2021) Possible link between
 496 Earth's rotation rate and oxygenation. *Nature Geoscience*.
 497 <https://doi.org/10.1038/s41561-021-00784-3>.

498 Klein, G.D. (1970) Depositional and dispersal dynamics of intertidal sand bars. *Journal of*
 499 *Sedimentary Research*, 40(4), 1095–1127.
 500 <https://doi.org/https://doi.org/10.1306/74D72144-2B21-11D7-8648000102C1865D>.

501 Klein, G.D. (1971) A Sedimentary Model for Determining Paleotidal Range. *Bulletin of the*
 502 *Geological Society of America*, 82(9), 2585–2592.
 503 [https://doi.org/https://doi.org/10.1130/0016-7606\(1971\)82\[2585:ASMFDP\]2.0.CO;2](https://doi.org/https://doi.org/10.1130/0016-7606(1971)82[2585:ASMFDP]2.0.CO;2).

- Kvale, E.P., Cutright, J., Bilodeau, D., Archer, A.E., Johnson, H.R. & Pickett, B. (1995) Analysis of modern tides and implications for ancient tidalites. *Continental Shelf Research*, 15(15), 1921–1943. [https://doi.org/10.1016/0278-4343\(95\)00001-H](https://doi.org/10.1016/0278-4343(95)00001-H).
- Lambeck, K. (1988) The earth's variable rotation: some geophysical causes. *Cambridge University Press*, 1–20. <https://doi.org/http://dx.doi.org/10.1017/CBO9780511569579>.
- Longhitano, S.G., Mellere, D., Steel, R.J. & Ainsworth, R.B. (2012) Tidal depositional systems in the rock record: A review and new insights. *Sedimentary Geology*, 279, 2–22. <https://doi.org/10.1016/j.sedgeo.2012.03.024>.
- McArthur, J.M., Algeo, T.J., van de Schootbrugge, B., Li, Q. & Howarth, R.J. (2008) Basinal restriction, black shales, Re-Os dating, and the Early Toarcian (Jurassic) oceanic anoxic event. *Paleoceanography*, 23(4). <https://doi.org/10.1029/2008PA001607>.
- Monteiro, F.M., Pancost, R.D., Ridgwell, A. & Donnadieu, Y. (2012) Nutrients as the dominant control on the spread of anoxia and euxinia across the Cenomanian-Turonian oceanic anoxic event (OAE2): Model-data comparison. *Paleoceanography*, 27(4). <https://doi.org/10.1029/2012PA002351>.
- Nielsen, H.L., Larsen, F. & Frandsen, N. (1989) Upper Triassic-Lower Jurassic tidal deposits of the Gassum Formation on Sjælland, Denmark. *Danmarks Geologiske Undersøgelse Serie A*, 23, 1–30. <https://doi.org/10.34194/seriea.v23.7043>.
- Ohkouchi, N., Kuroda, J. & Taira, A. (2015) The origin of Cretaceous black shales: A change in the surface ocean ecosystem and its triggers. *Proceedings of the Japan Academy Series B: Physical and Biological Sciences*, 91(7), 273–291. <https://doi.org/10.2183/pjab.91.273>.
- Oost, A. P., & Baas, J. H. (1994). The development of small scale bedforms in tidal environments: an empirical model for unsteady flow and its applications. *Sedimentology*, 41(5), 883-903. <https://doi.org/10.1111/j.1365-3091.1994.tb01430.x>
- Perez-Infante, J., Farrimond, P. & Furrer, M. (1996) *Global and local controls influencing the deposition of the La Luna Formation (Cenomanian-Carnpanian), western Venezuela. Chemical Geology*, Vol. 130.
- Price, D., Stuiver, C., Johnson, H., Gallego, A. & O'Hara Murray, R. (2016) The Scottish Shelf Model. part 4: east coast of Lewis and Harris sub-domain. *Scottish Marine and Freshwater Science*, 7(6), 147.
- Pugh, D.T. (1987) *Tides, surges and mean sea level*. John Wiley & Sons.

- Qiu, Z. & He, J. (2022) Depositional environment changes and organic matter accumulation of Pliensbachian-Toarcian lacustrine shales in the Sichuan basin, SW China. *Journal of Asian Earth Sciences*, 232. <https://doi.org/10.1016/j.jseaes.2021.105035>.
- Reineck, H.E. (1975). German North Sea Tidal Flats. In: Ginsburg, R.N. (eds) Tidal Deposits. Springer, Berlin, Heidelberg. https://doi.org/10.1007/978-3-642-88494-8_1
- Rust, B.R., Lawrence, D.A. & Zaitlin, B.A. (1989) The sedimentology and tectonic significance of Devonian and Carboniferous terrestrial successions in Gaspé, Quebec. *Atlantic Geology*, 25(1), 1–13. <https://doi.org/10.4138/1666>.
- Scotese, C.R. & Wright, N. (2018) PALEOMAP Paleodigital Elevation Models (PaleoDEMS) for the Phanerozoic PALEOMAP Project. <https://doi.org/https://www.earthbyte.org/paleodem-resourcescotese-and-wright-2018/>.
- Scourse, J.D., Austin, W.E.N., Long, B.T., Assinder, D.J. & Huws, D. (2002) Holocene evolution of seasonal stratification in the Celtic Sea: Refined age model, mixing depths and foraminiferal stratigraphy. *Marine Geology*, 191(3–4), 119–145. [https://doi.org/10.1016/S0025-3227\(02\)00528-5](https://doi.org/10.1016/S0025-3227(02)00528-5).
- Sellwood, B.W. (1972) Tidal-flat sedimentation in the Lower Jurassic of Bornholm, Denmark. *Palaeogeography, Palaeoclimatology, Palaeoecology*, 11(2), 93–106. [https://doi.org/https://doi.org/10.1016/0031-0182\(72\)90012-0](https://doi.org/https://doi.org/10.1016/0031-0182(72)90012-0).
- Shannon, L. V. & Nelson, G. (1996) The Benguela: Large Scale Features and Processes and System Variability. *The South Atlantic*, 163–210. https://doi.org/10.1007/978-3-642-80353-6_9.
- Sharples, J., Tweddle, J.F., Green, J.A.M., Palmer, M.R., Kim, Y.-N., Hickman, A.E., Holligan, P.M., Moore, C.M., Rippeth, T.P., Simpson, J.H. & Krivtsov, V. (2007) Spring-neap modulation of internal tide mixing and vertical nitrate fluxes at a shelf edge in summer. *Limnology and Oceanography*, 52(5). <https://doi.org/10.4319/lo.2007.52.5.1735>.
- Silva, R.L. & Duarte, L. v. (2015) Organic matter production and preservation in the Lusitanian Basin (Portugal) and Pliensbachian climatic hot snaps. *Global and Planetary Change*, 131, 24–34. <https://doi.org/10.1016/j.gloplacha.2015.05.002>.
- Simpson, J.H. & Bowers, D. (1981) Models of stratification and frontal movement in shelf seas. *Deep Sea Research Part A, Oceanographic Research Papers*, 28(7), 727–738. [https://doi.org/10.1016/0198-0149\(81\)90132-1](https://doi.org/10.1016/0198-0149(81)90132-1).

567 Simpson, J.H. & Bowers, D. (1984) The role of tidal stirring in controlling the seasonal heat
568 cycle in shelf seas. *Annales Geophysicae* (1983), 2(4), 411–416.

569 Simpson, J.H. & Hunter, J.R. (1974) Fronts in the Irish Sea. *Nature*, 250(2), 404–406.
570 <https://doi.org/https://doi.org/10.1038/250404a0>.

571 Slingerland, Rudy. (1986) Numerical computation of co-oscillating palaeotides in the Catskill
572 epeiric Sea of eastern North America. *Sedimentology*, 33(4), 487–497.
573 <https://doi.org/10.1111/j.1365-3091.1986.tb00756.x>.

574 Sparks, R.S.J., Bonnetaze, R.T., Huppert, H.E., Lister, J.R., Hallworth, M.A., Mader, H. &
575 Phillips, J. (1993) Sediment-laden gravity currents with reversing buoyancy. *Earth and*
576 *Planetary Science Letters*, 114(2–3), 243–257. [https://doi.org/10.1016/0012-](https://doi.org/10.1016/0012-821X(93)90028-8)
577 [821X\(93\)90028-8](https://doi.org/10.1016/0012-821X(93)90028-8).

578 Stammer, D., Ray, R.D., Andersen, O.B., Arbic, B.K., Bosch, W., Carrère, L., Cheng, Y., Chinn,
579 D.S., Dushaw, B.D., Egbert, G.D., Erofeeva, S.Y., Fok, H.S., Green, J.A.M., Griffiths, S.,
580 King, M.A., Lapin, V., Lemoine, F.G., Luthcke, S.B., Lyard, F., Morison, J., Müller, M.,
581 Padman, L., Richman, J.G., Shriver, J.F., Shum, C.K., Taguchi, E. & Yi, Y. (2014) Accuracy
582 assessment of global barotropic ocean tide models. *Reviews of Geophysics*, 52(3).
583 <https://doi.org/10.1002/2014RG000450>.

584 Stow, D.A.V. & Tabrez, A.R. (1998) Hemipelagites: processes, facies and model. *Geological*
585 *Society Special Publication*, 129, 317–337.
586 <https://doi.org/10.1144/GSL.SP.1998.129.01.19>.

587 Stow, D.A. V, Huc, A.-Y. & Bertrand, P. (2001) Depositional processes of black shales in deep
588 water. *Marine and Petroleum Geology*, 18, 491–498.
589 [https://doi.org/https://doi.org/10.1016/S0264-8172\(01\)00012-5](https://doi.org/https://doi.org/10.1016/S0264-8172(01)00012-5).

590 Takashima, R., Nishi, H., Yamanaka, T., Hayashi, K., Waseda, A., Obuse, A., Tomosugi, T.,
591 Deguchi, N. & Mochizuki, S. (2010) High-resolution terrestrial carbon isotope and
592 planktic foraminiferal records of the Upper Cenomanian to the Lower Campanian in the
593 Northwest Pacific. *Earth and Planetary Science Letters*, 289(3–4), 570–582.
594 <https://doi.org/10.1016/j.epsl.2009.11.058>.

595 Tanavsuu-Milkeviciene, K. & Plink-Bjorklund, P. (2009) Recognizing Tide-Dominated Versus
596 Tide-Influenced Deltas: Middle Devonian Strata of the Baltic Basin. *Journal of*
597 *Sedimentary Research*, 79(12), 887–905. <https://doi.org/10.2110/jsr.2009.096>.

598 Taylor, G.I. (1920) Tidal friction in the Irish Sea. *Proceedings of the Royal Society of London*
599 *Series A*, 96, 1–33. <https://doi.org/10.1098/rsta.1920.0001>

600 Tessier, B. (2023) Tidal rhythmites: Their contribution to the characterization of tidal
601 dynamics and environments. In: *A Journey Through Tides*. Elsevier, pp. 283–305.
602 <https://doi.org/10.1016/B978-0-323-90851-1.00015-7>.

603 Tessier, B. & Gigot, P. (1989) A vertical record of different tidal cyclicities: an example from
604 the Miocene Marine Molasse of Digne (Haute Provence, France). *Sedimentology*, 36(5),
605 767–776. <https://doi.org/https://doi.org/10.1111/j.1365-3091.1989.tb01745.x>.

606 Tovmasjana, K. (2013) *Depositional environment of the tidally-dominated transgressive*
607 *succession: Rezekne and Pärnu regional stages, Baltic Devonian Basin*. University of
608 Latvia, Latvia.

609 Tuerena, R.E., Williams, R.G., Mahaffey, C., Vic, C., Green, J.A.M., Naveira-Garabato, A.,
610 Forryan, A. & Sharples, J. (2019) Internal Tides Drive Nutrient Fluxes Into the Deep
611 Chlorophyll Maximum Over Mid-ocean Ridges. *Global Biogeochemical Cycles*, 33(8).
612 <https://doi.org/10.1029/2019GB006214>.

613 Uehara, K., Scourse, J.D., Horsburgh, K.J., Lambeck, K. & Purcell, A.P. (2006) Tidal evolution
614 of the northwest European shelf seas from the Last Glacial Maximum to the present.
615 *Journal of Geophysical Research: Oceans*, 111(9).
616 <https://doi.org/10.1029/2006JC003531>.

617 Waltham, D. (2015) Milankovitch Period Uncertainties and Their Impact on
618 Cyclostratigraphy. *Journal of Sedimentary Research*, 85, 990–998.

619 Ward, S.L., Scourse, J.D., Yokoyama, Y. & Neill, S.P. (2020) The challenges of constraining
620 shelf sea tidal models using seabed sediment grain size as a proxy for tidal currents.
621 *Continental Shelf Research*, 205. <https://doi.org/10.1016/j.csr.2020.104165>.

622 Way, M.J., Genio, A.D. Del, Kiang, N.Y., Sohl, L.E., David, H., Aleinov, I., Kelley, M. & Clune, T.
623 (2016) Was Venus the First Habitable World of our Solar System ? *Geophysical*
624 *Research Letters*, 43, 8376–8383. <https://doi.org/10.1002/2016GL069790>.

625 Wells, M.R., Allison, P.A., Hampson, G.J., Piggott, M.D. & Pain, C.C. (2005) Modelling ancient
626 tides: The Upper Carboniferous epi-continental seaway of Northwest Europe.
627 *Sedimentology*, 52(4), 715–735. <https://doi.org/10.1111/j.1365-3091.2005.00718.x>.

628 Wells, M.R., Allison, P.A., Piggott, M.D., Hampson, G.J., Pain, C.C. & Gorman, G.J. (2010)
629 Tidal modeling of an ancient tide-dominated seaway, part 1: Model validation and

- application to global early cretaceous (aptian) tides. *Journal of Sedimentary Research*, 80(5–6), 393–410. <https://doi.org/10.2110/jsr.2010.044>.
- Wendt, J., Kaufmann, B., Belka, Z., Farsan, N. & Karimi Bavandpur, A. (2004) Devonian/Lower Carboniferous stratigraphy, facies patterns and palaeogeography of Iran Part II. Northern and central Iran. *Acta Geologica Polonica*, 55(1), 31–97.
- Wignall, P.B. (1991) Model for transgressive black shales? *Geology*, 19(2), 167–170. [https://doi.org/10.1130/0091-7613\(1991\)019<0167:MFTBS>2.3.CO;2](https://doi.org/10.1130/0091-7613(1991)019<0167:MFTBS>2.3.CO;2).
- Wignall, P. B., & Newton, R. (2001). Black shales on the basin margin: a model based on examples from the Upper Jurassic of the Boulonnais, northern France. *Sedimentary Geology*, 144(3-4), 335-356. [https://doi.org/10.1016/S0037-0738\(01\)00125-7](https://doi.org/10.1016/S0037-0738(01)00125-7)
- Williams, G.E. (2000) Geological constraints on the Precambrian history of Earth's rotation and the Moon's orbit. *Reviews of Geophysics*, 38, 37–59. <https://doi.org/10.1029/1999RG900016>
- Wilmes, S. -B., Green, J.A.M. & Schmittner, A. (2021) Was vertical mixing in the glacial ocean enhanced? *Nature Communications Earth and Environment*, 2(166). <https://doi.org/10.1038/s43247-021-00239-y>
- Wilmes, S.-B. & Green, J.A.M. (2014) The evolution of tides and tidal dissipation over the past 21,000 years. *Journal of Geophysical Research: Oceans*, 119(7). <https://doi.org/10.1002/2013JC009605>.
- Wunsch, C. & Ferrari, R. (2004) Vertical mixing, energy, and the general circulation of the oceans. *Annual Review of Fluid Mechanics*, 36(1), 281–314. <https://doi.org/10.1146/annurev.fluid.36.050802.122121>.
- Yang, J., Boué, G., Fabrycky, D.C. & Abbot, D.S. (2014) Strong dependence of the inner edge of the habitable zone on planetary rotation rate. *Astrophysical Journal Letters*, 787(1). <https://doi.org/10.1088/2041-8205/787/1/L2>.
- Zand-Moghadam, H., Moussavi-Harami, R. & Mahboubi, A. (2014) Sequence stratigraphy of the Early-Middle Devonian succession (Padeha Formation) in Tabas Block, East-Central Iran: Implication for mixed tidal flat deposits. *Palaeoworld*, 23(1), 31–49. <https://doi.org/10.1016/j.palwor.2013.06.002>.
- Zaron, E.D. & Egbert, G.D. (2006) Estimating Open-Ocean Barotropic Tidal Dissipation: The Hawaiian Ridge. *Journal of Physical Oceanography*, 36(6), 1019–1035. <https://doi.org/https://doi.org/10.1175/JPO2878.1>.

662 Zuchuat, Valentin., Steel, Elisabeth., Mulligan, R.P., Collins, D.S. & Green, J.A.Mattias. (2022)
663 Tidal dynamics in palaeo-seas in response to changes in physiography, tidal forcing and
664 bed shear stress. *Sedimentology*, 69(4), 1861–1890.
665 <https://doi.org/10.1111/sed.12975>.
666
667

Figure captions

Figure 1: The palaeogeographic reconstructions and the location of tidal proxies for (a) 400 Ma; (b) 185 Ma; (c) 95 Ma, with the specifics of direct proxies (DP) and black shales (BS)

Figure 2: (a) The simulated M₂ tidal amplitudes in metres for the PD control simulations; (b) The simulated S₂ tidal amplitudes.

Figure 3: (a) Simulated M₂ tidal amplitudes; (b) Simulated S₂ tidal amplitudes; (c) Simulated mean spring tidal range for 400 Ma, calculated by $2(\eta_{M_2} + \eta_{S_2})$, and the marked palaeotidal range proxies; (d) close-up of ocean region surrounding Laurussia.

Figure 4: The tidal range indicated by direct proxies and the corresponding model prediction for 400 Ma. The modelled tidal range is the range in the gridcell nearest to the proxy location, where the error bar shows the largest and smallest values in a 3x3 grid box centered on the proxy location.

Figure 5: a) Simulated mean spring tidal amplitudes for the 185 Ma time slice; (b) close-up of the Laurasian Sea Way where the proxies are located.

Figure 6: The M₂ tidal range indicated by direct proxies and the corresponding model prediction for 185 Ma. Note that in this figure, DP4 has been moved from the original location on land to the nearest coastal ocean grid cell.

Figure 7: Predicted Simpson-Hunter criterion for 185 Ma, and the palaeo-location of black shale proxies.

Figure 8: a) Simulated M₂ tidal amplitudes; (b) Simulated M₂ tidal current magnitude for the 95 Ma time slice. For clarity, the proxy locations are marked in Figure 9.

Figure 9: Predicted Simpson-Hunter criterion for 95 Ma, and the palaeo-location of black shale proxies.

700

701

Table 1: Forcing parameters used in the model simulations, with data from Daher et al. (2021). The M2 forcing factor is based on the change in lunar distance associated with the change in orbital periods. The K1 forcing factor is made up of 2/3 from the Moon and 1/3 from the Sun.

Time slice (Ma)	Sidereal day	M ₂ period [hrs]	S ₂ period [hrs]	K ₁ period (hrs)	M ₂ forcing factor	K ₁ forcing factor
400	21.95	11.01	10.58	21.95	1.11	1.07
185	23.19	11.77	11.35	23.19	1.05	1.03
95	23.49	12.18	11.78	23.49	1.01	1.01
PD	23.93	12.42	12.00	23.93	1.00	1.00

Table 2: The model prediction of Simpson-Hunter criterion (X) and associated stratification state for the 185 Ma time slice

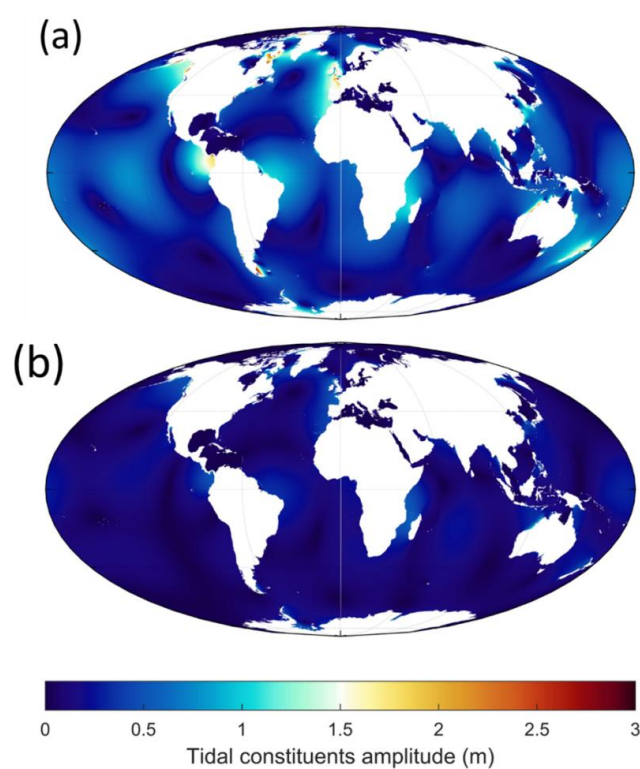
	BS1	BS2	BS3	BS4	BS5
$\log_{10} \chi$	2.0	3.8	7.9	4.1	8.0
Water column structure	mixed	stratified	stratified	stratified	stratified

713 Table 3: The model prediction of Simpson-Hunter criterion (logarithms to 10) and the
 714 associated tidal stratification for 95 Ma. Note that we expect the locations of black shales to
 715 sit in a stratified water column.

	BS6	BS7	BS8	BS9	BS10	BS11	BS12	BS13
$\log_{10} \chi$	3.2	3.6	5.1	6.0	2.0	3.3	1.8	2.5
Water column structure	Stratified	stratified	stratified	stratified	mixed	stratified	mixed	stratified

716

717



718

719 Figure 1: The palaeogeographic reconstructions and the location of tidal proxies for (a) 400
720 Ma; (b) 185 Ma; (c) 95 Ma, with the specifics of direct proxies (DP) and black shales (BS)

721

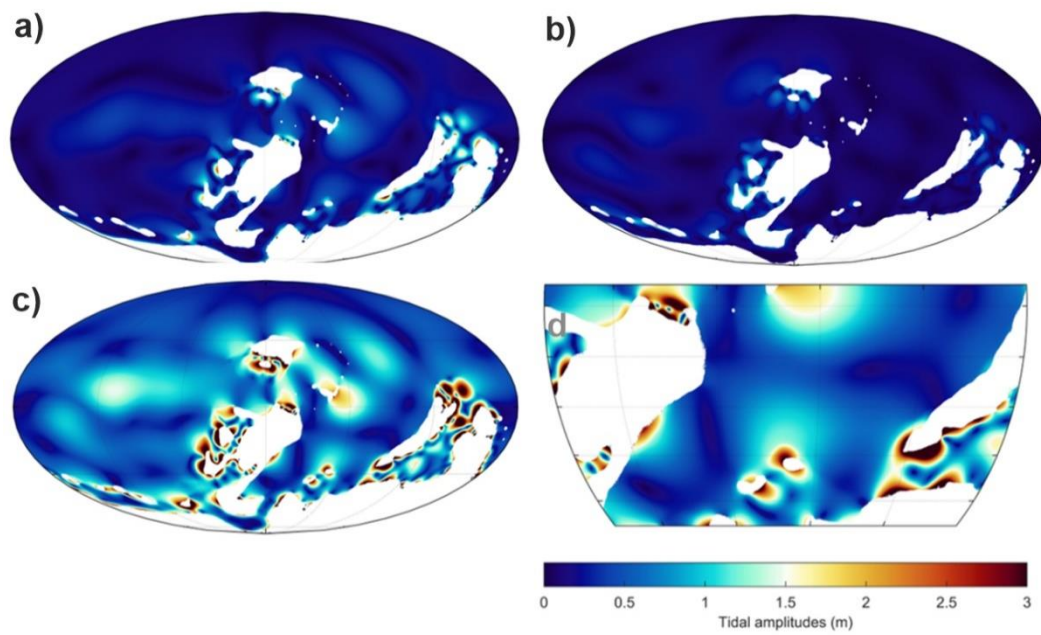
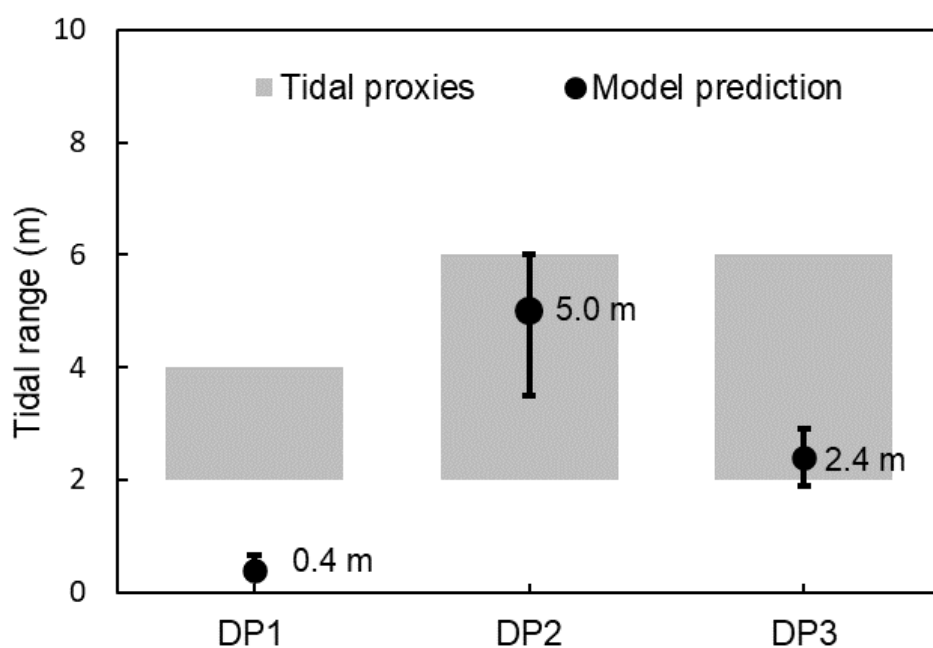


Figure 3: (a) Simulated M2 tidal amplitudes; (b) Simulated S2 tidal amplitudes; (c) Simulated mean spring tidal range for 400 Ma, calculated by $2(\eta M2 + \eta S2)$, and the marked palaeotidal range proxies; (d) close-up of ocean region surrounding Laurussia.

733



734

735 Figure 4: The tidal range indicated by direct proxies and the corresponding model prediction
 736 for 400 Ma. The modelled tidal range is the range in the gridcell nearest to the proxy
 737 location, where the error bar shows the largest and smallest values in a 3x3 grid box
 738 centered on the proxy location.

739

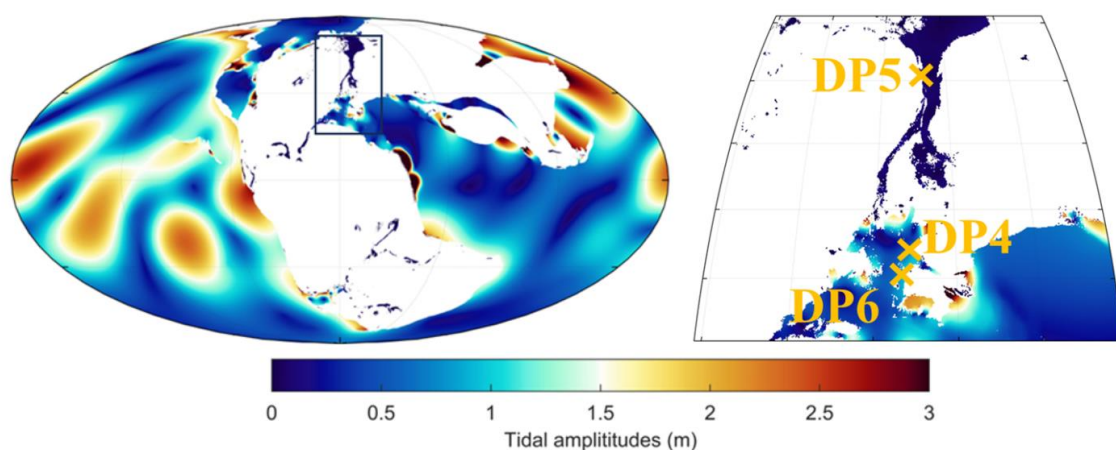


Figure 5: a) Simulated mean spring tidal amplitudes for the 185 Ma time slice; (b) close-up of the Lurasian Sea Way where the proxies are located.

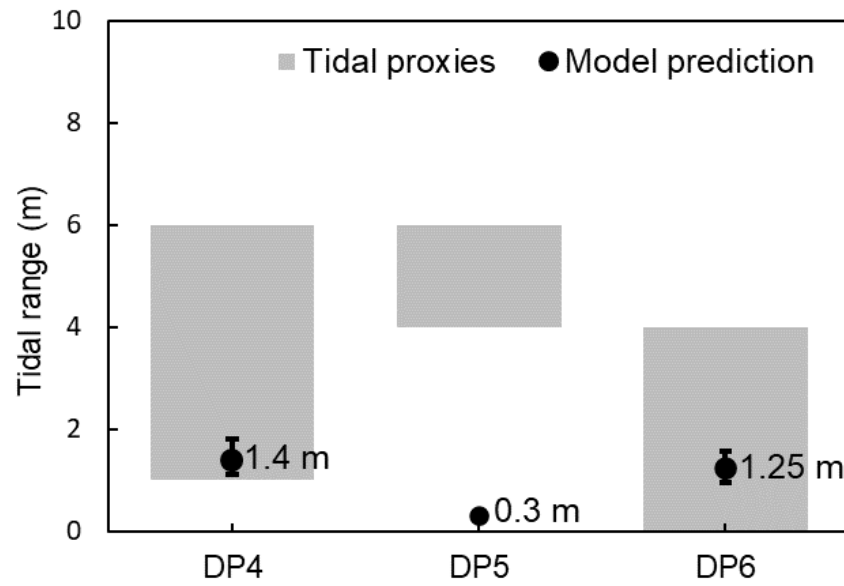


Figure 6: The M-2 tidal range indicated by direct proxies and the corresponding model prediction for 185 Ma. Note that in this figure, DP4 has been moved from the original location on land to the nearest coastal ocean grid cell.

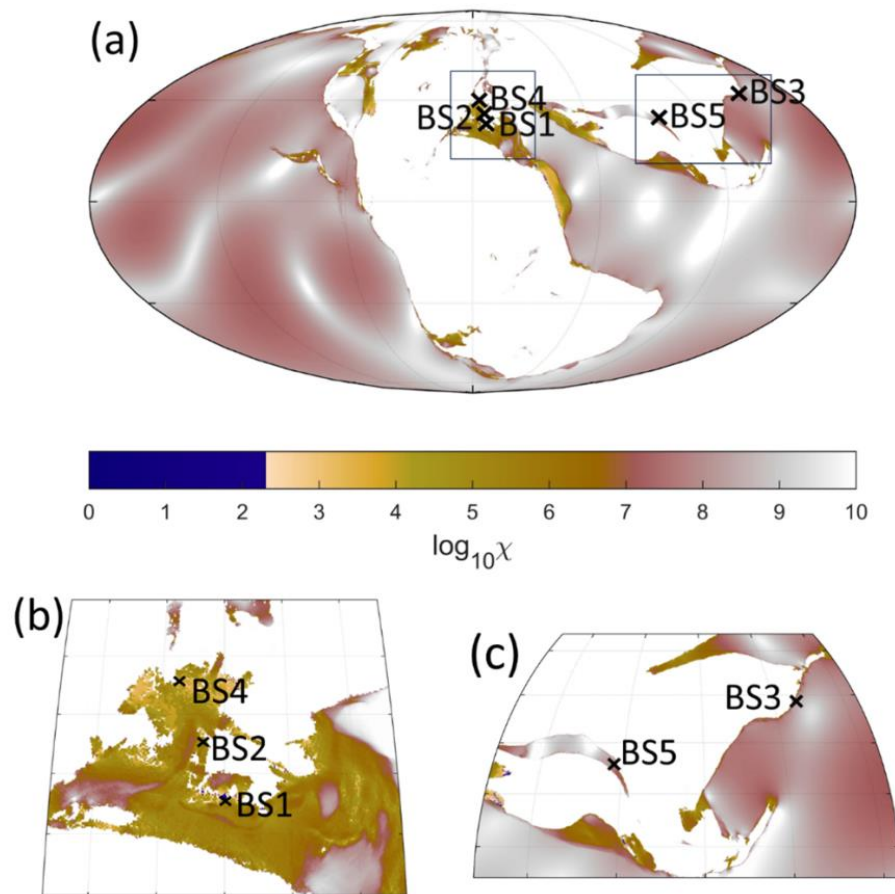
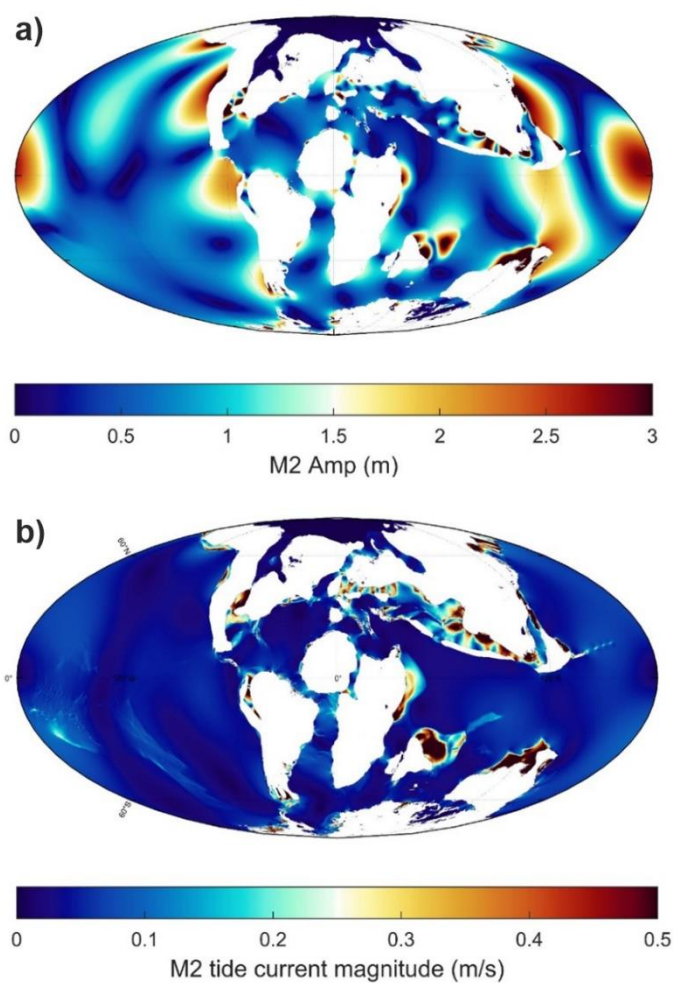


Figure 7: Predicted Simpson-Hunter criterion for 185Ma, and the palaeo-location of black shale proxies.

755



756

757 Figure 8: a) Simulated M2 tidal amplitudes; (b) Simulated M2 tidal current magnitude for the
758 95 Ma time slice. For clarity, the proxy locations are marked in Figure 9.

759

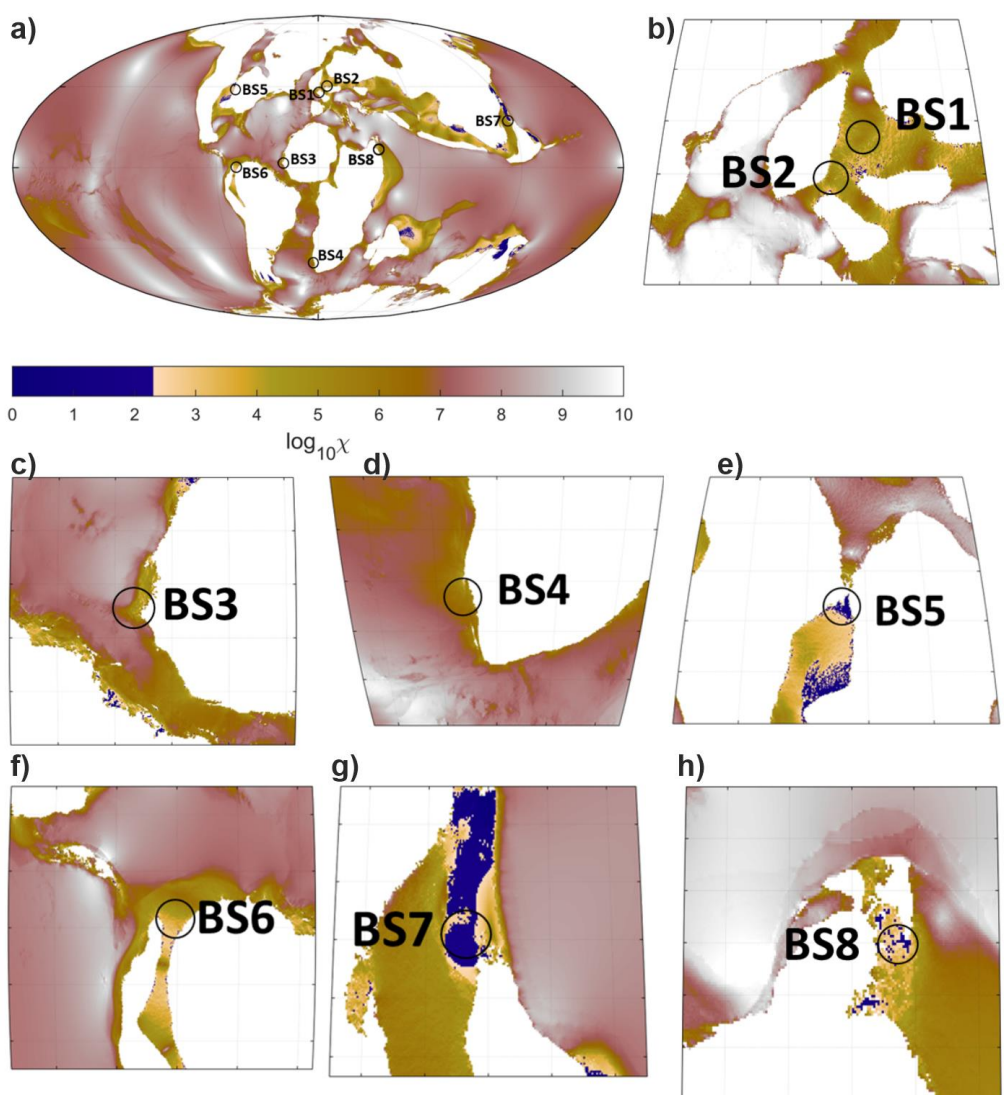


Figure 9: Predicted Simpson-Hunter criterion for 95 Ma, and the palaeo-location of black shale proxies.